

Article

Design and Modeling of a Bio-Inspired Compound Continuum Robot for Minimally Invasive Surgery

Gang Zhang ^{1,2} , Fuxin Du ^{1,2,3,*}, Shaowei Xue ¹, Hao Cheng ¹, Xingyao Zhang ¹, Rui Song ⁴ and Yibin Li ⁴

- ¹ School of Mechanical Engineering, Shandong University, Jinan 250100, China; gangzhang@mail.sdu.edu.cn (G.Z.); shaowei_xue@mail.sdu.edu.cn (S.X.); haocheng@mail.sdu.edu.cn (H.C.); zhangxingyao@mail.sdu.edu.cn (X.Z.)
- ² Key Laboratory of High Efficiency and Clean Mechanical Manufacture of Ministry of Education, Shandong University, Jinan 250061, China
- ³ Beijing Advanced Innovation Center for Intelligent Robots and Systems, Beijing Institute of Technology, Beijing 100811, China
- ⁴ School of Control Science and Engineering, Shandong University, Jinan 250100, China; rsong@sdu.edu.cn (R.S.); liyb@sdu.edu.cn (Y.L.)
- * Correspondence: dufuxin@sdu.edu.cn

Abstract: The continuum robot is a new type of bionic robot which is widely used in the medical field. However, the current structure of the continuum robot limits its application in the field of minimally invasive surgery. In this paper, a bio-inspired compound continuum robot (CCR) combining the concentric tube continuum robot (CTR) and the notched continuum robot is proposed to design a high-dexterity minimally invasive surgical instrument. Then, a kinematic model, considering the stability of the CTR part, was established. The unstable operation of the CCR is avoided. The simulation of the workspace shows that the introduction of the notched continuum robot expands the workspace of CTR. The dexterity indexes of the robots are proposed. The simulation shows that the dexterity of the CCR is 1.472 times that of the CTR. At last, the length distribution of the CCR is optimized based on the dexterity index by using a fruit fly optimization algorithm. The simulations show that the optimized CCR is more dexterous than before. The dexterity of the CCR is increased by 1.069 times. This paper is critical for the development of high-dexterity minimally invasive surgical instruments such as those for the brain, blood vessels, heart and lungs.

Keywords: compound continuum robot; concentric tube continuum robot; notched continuum robot; dexterity



Citation: Zhang, G.; Du, F.; Xue, S.; Cheng, H.; Zhang, X.; Song, R.; Li, Y. Design and Modeling of a Bio-Inspired Compound Continuum Robot for Minimally Invasive Surgery. *Machines* **2022**, *10*, 468. <https://doi.org/10.3390/machines10060468>

Academic Editors: Yanjie Wang, Xiaofeng Liu, Aihong Ji, Shichao Niu and Bo Li

Received: 18 April 2022

Accepted: 9 June 2022

Published: 11 June 2022

Publisher's Note: MDPI stays neutral with regard to jurisdictional claims in published maps and institutional affiliations.



Copyright: © 2022 by the authors. Licensee MDPI, Basel, Switzerland. This article is an open access article distributed under the terms and conditions of the Creative Commons Attribution (CC BY) license (<https://creativecommons.org/licenses/by/4.0/>).

1. Introduction

The powerful locomotion capability of biologically inspired continuum robots in small spaces has attracted increasing attention from researchers [1–4]. As shown in Figure 1, this robot achieves extreme dexterity through the biological structure of bionic snakes, octopus tentacles and elephant trunks.

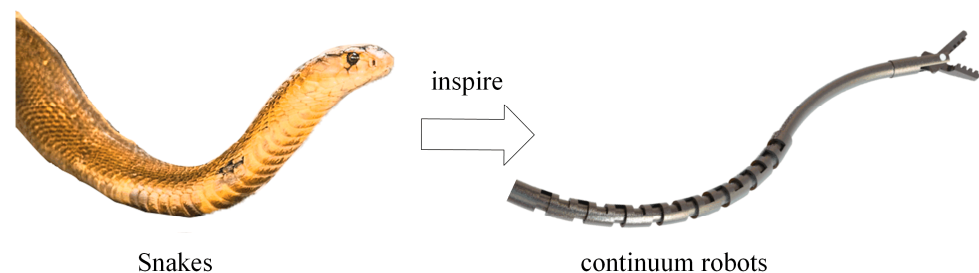


Figure 1. Bio-inspired continuum robot.

The ultra-high dexterity makes the continuum robot widely used in various fields of medicine such as laparoscopy and thoracoscopy [5–7]. However, with the development of minimally invasive surgery, the requirements for surgical instruments have become stricter. The instruments are required to bypass human organs or tissues to perform operations deeper in the human body, such as transeptal puncture, vascular surgery and skull base surgery [8,9]. While maintaining high dexterity, continuum robots with smaller diameters and a larger central access are required in these procedures.

Continuum robots were first built in the 1960s. After the 2000s, with the clarification of the application scenarios of continuum robots, related research has gradually increased. The application in the medical field has greatly promoted the research and development process of continuum robots [10,11]. In the past 10 years, many continuum robots have been proposed; these continuum robots have obvious trade-offs between the size of the center channel and the size of the continuum robot. By imitating the bones of snakes, a continuum robot composed of hinged joints was proposed by Li [12–14]. This robot has excellent dexterity, but the existence of the hinge narrows the central channel and limits the use of end instruments. A continuum robot composed of discrete joints and a central rod was proposed by Simaan [15,16]. Although this structure has unique advantages in terms of accuracy and stiffness, the central rod of this continuum limits the end instruments. To solve the problem of the tiny central channel, Murphy et al. [17–19] proposed a notched continuum robot (NCR). This kind of continuum robot replaces the hinge joints of the hinged-joints continuum robot by machining notches on the Nitinol tube in order to obtain a more significant central channel. NCRs have good stiffness and motion accuracy. In subsequent studies, this notched continuum robot has been used in laryngeal surgery [20], pediatric vascular surgery [21] and other aspects. However, similar to the hinged-joints continuum robot, the diameter of the robot is limited to the millimeter level. In 2009, Webster et al. [22] proposed a concentric tube robot (CTR) made of a nested pre-bent Nitinol tube. By eliminating the drive cable, the diameter of the robot can easily reach sub-millimeters. The surgical instruments can be made smaller in size. This special continuum robot has been used in skull base tumor resection [23], cardiac intervention [24], lung biopsy [25], etc. Although the CTR can achieve a satisfactory diameter, Alfalahi et al. [26] pointed out an apparent trade-off between the stiffness of the CTR and the working space. The stiffness of this robot is mainly determined by the material, which makes it difficult to change. Therefore, the workspace of the CTR with the same configuration is smaller than that of the NCR.

Other kinds of continuum robots have also been further developed. Fluid-driven and magnetic-field-driven continuum robots are a research hotspot. The fluid-driven continuum robot has excellent flexibility and a great turning angle. Such robots have been intensively studied by Greer and Laschi et al. [27,28]. Miniaturization and safety issues are the keys to hindering the application of fluid-driven continuum robots in surgery. There is a risk of rupture of the fluid bag when moving near scalpels. Magnetic-field-driven continuum robots can obtain a satisfactory diameter. However, such continuum robots have limitations in terms of biocompatibility and flexibility [1]. All in all, there are still many problems to be solved in the application of these two continuum robots in surgery.

Mixing different forms of continuum robots to improve the performance of robots has attracted the attention of researchers. The cable-driven continuum robot and CTR can complement each other's shortcomings. The cable drive continuum increases the CTR's workspace. The CTR reduces the size of cable-driven continuum robots. In 2017, the initial concept of a hybrid-actuated continuum robot was proposed by Li [29]. Li proposed the combination of a cable-driven continuum with a CTR. The dexterity of this continuum robot was evaluated. Li's paper is very instructive. However, Li did not consider the application limitations of this continuum robot, especially in terms of the size. In 2021, Abdel-Nasser [30] proposed the use of an articulated continuum robot combined with a CTR for use in minimally invasive surgery. Abdel-Nasser's research shows that the hybrid-actuated continuum robots have a greater workspace and dexterity. However, not

all types of cable-driven continuum robots are suitable for being combined with CTR. The diameter of the articulated continuum robot is too large to be applied in minimally invasive surgery. Moreover, Li and Abdel-Nasser did not consider the stability issues of the CTR part when the cable-driven continuum robot part is in a state of high curvature. It should be noted that instability refers to the rapid jump of the concentric tube robot from one equilibrium position with higher potential energy to another equilibrium point with lower potential energy. This movement is difficult to control and is extremely dangerous for surgical procedures [31,32]. In the design, we need to try to avoid this situation.

This paper proposed a compound continuum robot combining the CTR and the NCR which can achieve a smaller diameter and a larger central cavity. The possible stability issues of the CCR are considered. Compared with CCRs proposed in previous studies, the CCR proposed in this article is more suitable for minimally invasive surgery. The contributions can be summarized as follows:

- A compound continuum robot (CCR) combining the concentric tube continuum robot (CTR) and the notched continuum robot is proposed to design high-dexterity minimally invasive surgical instruments. The simulations show that the CCR's workspace is bigger than that of the CTR and that the dexterity indices of the CCR are 1.231 times larger than those of the CTR.
- Stability issues in the CTR part were considered. The failure boundaries of the workspace are defined. In the newly defined workspace, the CCR can perform stable movements. The CTR section avoids instability.
- The dexterity index of the CCR is proposed. The length distribution of the compound continuum robot is optimized using a fruit fly algorithm based on the dexterity index.

The rest of the paper is as follows. Section 2 elaborates on the critical issues of this paper. Section 3 summarizes the methods and calculations used in this paper. Section 4 simulates the workspace and dexterity of the CCR and discusses the obtained results. Section 5 summarizes the whole paper.

2. Problem Formulation

Miniaturization and dexterity have been the focus of research on microsurgical instruments. The excellent adaptability and dexterity of the continuum robot make it widely used in surgical instruments. In the past decade, continuum robots have been widely adopted in laparoscopy and thoracoscopy. With the advancement of technology, minimally invasive surgery has gradually developed into deeper areas of the human body that are more difficult to reach with traditional minimally invasive surgery, such as the skull base, heart and lungs, as shown in Figure 2. These operations not only require the extremely high dexterity of surgical instruments but also have strict requirements as to the peripheral diameter of the surgical instruments and the diameter of the central cavity. The importance of the diameter is obvious. During the design stage, the importance of the cavity in the center of a surgical instrument is often overlooked. However, in the actual surgical process, it is very unlikely that only one instrument is used, and the existence of the central cavity exists to realize the replacement of these surgical instruments.

However, it is difficult to reduce the diameter and increase the diameter of the central cavity of the cable-driven continuum robots. The emergence of the concentric tube robot is a turning point in terms of the miniaturization of the continuum robot. The design of the cable drive is canceled in CTR. It completes the dexterous movement by advancing and rotating the pre-bent elastic tube. This design provides a large central channel for surgical tools, and the diameter can be easily reduced by using flexible tubes with small diameters. The CTR's invariable curvature cable-driven continuum robot leads to a smaller working space and minimizes the dexterity compared with the cable-driven continuum robot. Some researchers found that the defects of continuum robots can be overcome by combining different continuum robots. However, the current design of the compound continuum robot is still at the theoretical stage. Neither the small diameter nor the large central lumen of the surgical instruments required in actual surgery are discussed. A feasible solution still

needs to be devised. As shown in Figure 2, in this paper, a biomimetic excitation composite continuum robot with high dexterity and a small diameter and large central cavity is proposed. This special continuum robot has broad application prospects in surgical robots. Meanwhile, like ordinary continuum mechanisms, the CCR can also provide a solution for the development of dexterous and manual small instruments.

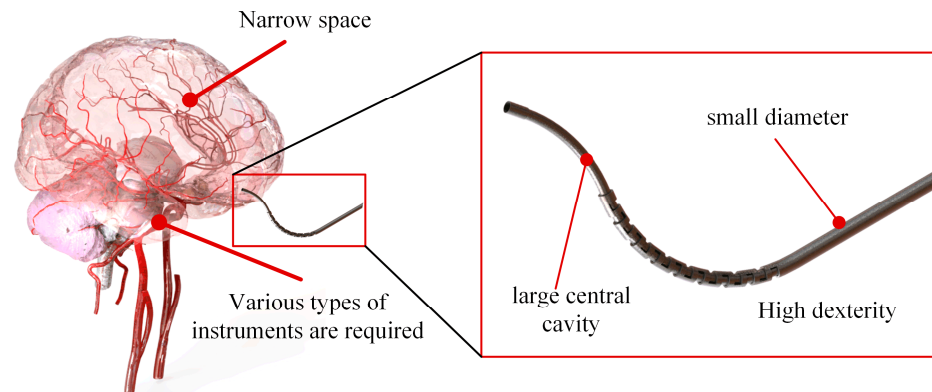


Figure 2. Requirements for surgical instruments in surgery.

3. Methods

This section summarizes the methods and theories used in this paper. The motion mechanism was expounded, and the kinematic model of the CCR was established. The stability condition of the CCR was introduced as the boundary condition of the workspace. Then, a posture dexterity evaluation method was introduced to evaluate the dexterity index of the CCR. Finally, a fruit fly algorithm was used to optimize the length assignments for continuum robots.

3.1. Design and Mechanism of Compound Continuum Robot

Keeping a large central cavity in the small size of the continuum robot is one of the key factors that hinder designers. The traditional processing methods make it difficult for ordinary cable-driven continuum robots to meet the requirements of operations in small spaces such as the skull base and heart. In the process of research, we found that the combination of the NCR and CTR not only circumvents the shortcomings of each but also meets physicians' expectations for a new generation of surgical instruments, as shown in Figure 3.

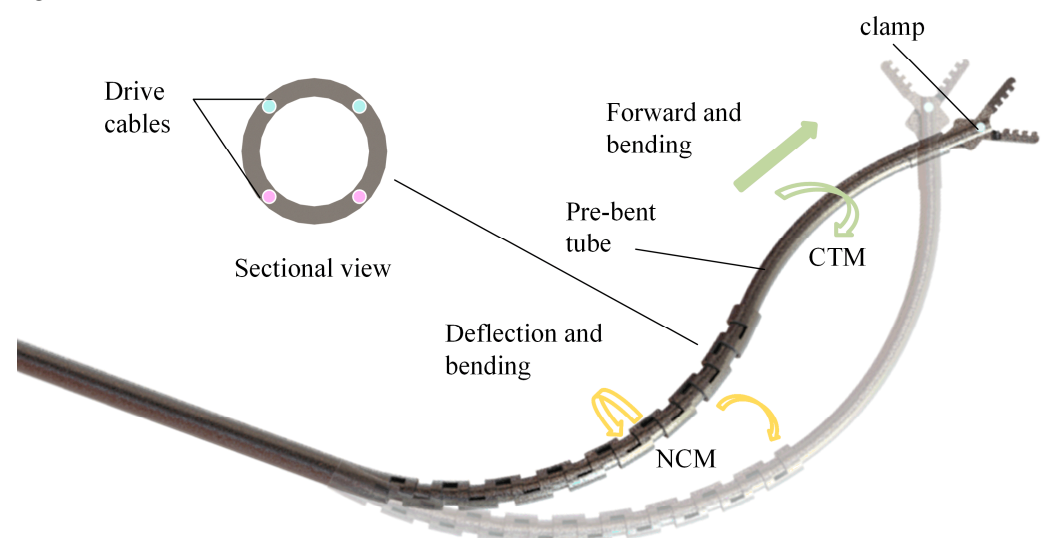


Figure 3. A bio-inspired continuum robot compound composed of a CTR with an NCR.

Femtosecond laser machined Nitinol tubes can be used as NCR parts. The tube wall needs to be pre-machined with four through holes through which the drive cables are to pass. The CTR part is a curved Nitinol tube with a curvature that is set in advance. The 3D printing of elastic materials to process the CCR is also an ideal processing method.

The CCR is divided into three parts: the NCR part, the CTR part and the surgical instrument part. The NCR has degrees of freedom in rotation and bending. The bending degree of freedom of the NCR is achieved by two pairs of antagonistic filaments, and the rotational degree of freedom is achieved by the rotation of the straight tube. The CTR has a unique operating mechanism with degrees of freedom for feed and rotation. The feeding of the CTR releases the elastic potential energy accumulated by the pre-bent tube, thereby enabling bending. The curvature of the CTR, without releasing the elastic potential energy, will be limited to the curvature of the NCR portion. Figure 3 shows the clamps commonly used in surgery. The surgical clamps were passed through the cavity of the CTR section. When an instrument needs to be replaced, the clamp can be pulled out along the cavity, and a new surgical instrument can be inserted through the cavity.

Before the combination, the NCR was able to obtain a large working space, and the size was difficult to reduce. The CTR enables smaller diameters but less flexibility and a smaller workspace. Both have a larger central cavity. After bonding, the larger central cavity is preserved. The robot's dexterity and minimum size constraints are lifted.

3.2. Kinematics Model and Smooth-Running Workspace

Based on the piecewise constant curvature hypothesis proposed by Hannan and Walker [33] et al., the kinematic model of the composite continuum can be established. It assumes that the curvatures of all the points of the continuum robot backbone are equal constants. As shown in Figure 4, the parameters of the CCR are defined. The skeleton curves of NCR and CTR can be regarded as two arcs. We stipulate that the constant length of the NCR part is L_1 , the bending angle is θ_1 and the rotation angle is φ_1 . The variable length of the CTR part is L_2 , the bending angle is θ_2 , the rotation angle is φ_2 and the fixed curvature is k . The parameter θ_2 is related to the invariant parameter k , and the relationship between θ_2 and k is as follows.

$$\theta_2 = kL_2 \quad (1)$$

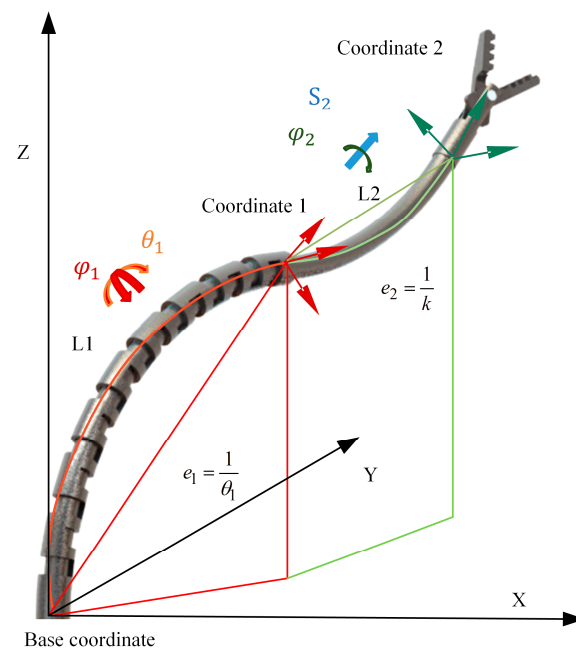


Figure 4. The backbone curve and coordinates of the CCR.

The NCR part can be abstracted into a circular tube, as shown in Figure 5. The effect of incisions on the NCR on the shape of the NCR backbone was not considered when the number of incisions was sufficient. The yellow and blue rods represent the cables that drive the NCR. The amount of change (θ) of each parameter in the joint space of the NCR part is driven by the change in the cable length in the drive space (l).

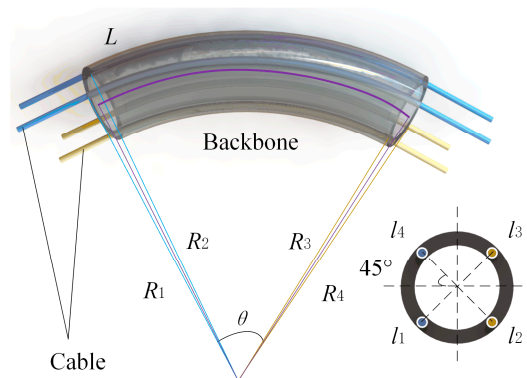


Figure 5. The relationship between the cable length and angle of the NCR.

Set the yellow cable as cable 1 and cable 2, the blue cable as cable 3 and cable 4 and the bending radius of each cable as R_i . i refers to the i -th cable. There is 45° spacing between the cables.

According to Figure 5, the radius of the backbone (R_0) of the NCR can be expressed by:

$$R_0 = L/\theta \tag{2}$$

According to the geometric relationship in Figure 5, the length of each cable can be obtained.

$$l_i = \theta R_i \tag{3}$$

$$R_i = R_N \mp \sqrt{2}d/4 \tag{4}$$

Use minus when i is 1 or 2 and plus when i is 3 or 4.

The length of the CTR parts is $L_2 = [0, L_{2max}]$. Taking the fixed end of the NCR as the basic coordinate system, the DH parameters of the CCR can be obtained, as shown in Table 1:

Table 1. CCR’s D-H parameters.

D-H Parameters	θ	a	α	d
NCR parts	φ_1	$L_1 \sin \theta_1 / \theta_1$	θ_1	$L_1(1 - \cos \theta_1) / \theta_1$
CTR parts	$\pi/2$ $\sin L_2/k$	0 kL_2	φ_2 $(1 - \cos kL_2)/k$	0 $\sin kL_2/k$

Bring it into the following homogeneous change matrix:

$$T_{i-1}^i = \begin{bmatrix} c\theta_i & -s\theta_i c\alpha_i & s\theta_i s\alpha_i & a_i c\theta_i \\ s\theta_i & c\theta_i c\alpha_i & -c\theta_i s\alpha_i & a_i s\theta_i \\ 0 & s\alpha_i & c\alpha_i & d_i \\ 0 & 0 & 0 & 1 \end{bmatrix} \tag{5}$$

In Equation (5), $c\theta_i = \cos \theta_i$, $s\theta_i = \sin \theta_i$, $c\alpha_i = \cos \alpha_i$, $s\alpha_i = \sin \alpha_i$.

By multiplying the homogeneous change matrices of each joint in turn, the end pose matrix T_z of the CCR can be solved, as shown in Equation (6).

$$T_z = T_0^1 T_1^2 T_2^3 = \begin{pmatrix} R_z & P_z \\ 0 & 1 \end{pmatrix} = \begin{pmatrix} R_{11} & R_{12} & R_{13} & P_1 \\ R_{21} & R_{22} & R_{23} & P_2 \\ R_{31} & R_{32} & R_{33} & P_3 \\ 0 & 0 & 0 & 1 \end{pmatrix} \tag{6}$$

$$\begin{aligned} R_{11} &= -c\theta_2(s\varphi_1s\varphi_2 - c\theta_1c\varphi_1c\varphi_2) - s\theta_2c\varphi_1s\theta_1, R_{21} = c\theta_2(c\varphi_1s\varphi_2 - c\theta_1s\varphi_1c\varphi_2) - s\theta_2s\varphi_1s\theta_1, \\ R_{31} &= -s\theta_2c\theta_1 - c\theta_2c\varphi_2s\theta_1, R_{12} = -c\varphi_1c\varphi_2 - c\theta_1c\varphi_1s\varphi_2, R_{22} = c\varphi_1c\varphi_2 - c\theta_1s\varphi_1s\varphi_2, \\ R_{32} &= s\theta_2(c\varphi_1s\varphi_2 + c\theta_1s\varphi_1c\varphi_2) + c\theta_2s\varphi_1s\theta_1, R_{13} = c\theta_2c\varphi_1s\theta_1 - s\theta_2(s\varphi_1s\varphi_2 - c\theta_1c\varphi_1c\varphi_2), \\ R_{23} &= s\theta_2(c\varphi_1s\varphi_2 + c\theta_1s\varphi_1c\varphi_2) - c\theta_2s\theta_1s\varphi_1, R_{33} = c\theta_2c\theta_1 - s\theta_2c\varphi_2s\theta_1, P_1 = \frac{1}{k}((c\theta_2 - 1) \\ &(s\varphi_1s\varphi_2 + c\theta_1c\varphi_1c\varphi_2) + s\theta_2s\theta_1c\varphi_1) - \frac{1}{\theta_1}L_1c\varphi_1(c\theta_1 - 1), P_2 = \frac{-1}{k}((c\theta_2 - 1)(c\varphi_1s\varphi_2 + c\theta_1s\varphi_1c\varphi_2) - \\ &s\theta_2s\theta_1s\varphi_1) - \frac{1}{\theta_1}L_1s\varphi_1(c\theta_1 - 1), P_3 = \frac{1}{k}((c\theta_2 - 1)s\theta_1c\varphi_2 + s\theta_2c\theta_1) + \frac{1}{\theta_1}L_1s\theta_1, \theta_2 = kL_2. \end{aligned}$$

In the same way, the forward kinematics model of the two-segment NCR and the forward kinematics model of the two-segment CTR can be solved. The DH parameters are shown in Tables 2 and 3.

Table 2. NCR’s D-H parameters.

D-H Parameters	i	θ	a	α	d
Segment 1	1	φ_1	$L_1\sin\theta_1/\theta_1$	θ_1	$L_1(1 - \cos\theta_1)/\theta_1$
Segment 2	2	$\pi/2$	0	φ_2	0
	3	$-\pi/2$	$L_2\sin\theta_2/\theta_2$	θ_2	$L_2(1 - \cos\theta_2)/\theta_2$

Table 3. CTR’s D-H parameters.

D-H Parameters	i	θ	a	α	d
Segment 1	1	φ_1	sink_1S_1/k_1	k_1S_1	$(1 - \cos k_1S_1)/k_1$
Segment 2	2	$\pi/2$	0	φ_2	0
	3	$-\pi/2$	sink_2S_2/k_2	k_2S_2	$(1 - \cos k_2S_2)/k_2$

Where φ_1 and φ_2 are the rotation angles of the first segment and the second segment of the NCR, L_1 and L_2 are the lengths of the first and second segments of the NCR and θ_1 and θ_2 are the bending angles of the first and second segments of the NCR.

S_1 and S_2 are the feed movements of the CTR’s first and second sections. k_1 and k_2 are the curvatures of the first and second segments of the CTR.

The CTR part is a pre-curved tube with a fixed curvature. When the NCR part bends, the curvature of the CTR part nested in the NCR part is changed. The elastic force caused by the changing curvature of the CTR part acts on the tube wall of the NCR part. When this curvature change is greater than the maximum allowable changing curvature, the elastic force causes stability problems in the CTR part. As shown in Figure 6, the stability problem refers to a sudden change in the movement speed of the CTR part when the CTR part is driven to rotate. The CTR part jumps rapidly from one point (usually a high-potential stabilization point) to another (usually a low-potential stabilization point).

The condition that the CTR is partially stable is introduced to correct the kinematics. The relevant theory proposed by Xu and Dupont [34,35] is used to construct the stability boundary conditions of the CCR. The theory is constructed based on the principle of least potential energy.

$$L_c\sqrt{r} < \arctan\left(\frac{K_1 + K_2}{(K_1l_2 + K_2l_1)\sqrt{r}}\right) \tag{7}$$

$$r = (1 + v)\|u_1\|\|k\| \tag{8}$$

$$v = \frac{k_{2xy}}{k_{2z}} - 1 \tag{9}$$

Among them, L_c is the length of the curved part of the concentric tube, K_1 and K_2 are the stiffnesses of each tube and l_1 and l_2 are the lengths of the straight part of each tube. u_1 is the curvature of the current NCR part. k_{2xy} is the bending stiffness, and k_{2z} is the torsional stiffness. The Newton iteration method was used to solve Equation (7).



Figure 6. Stability issues of the CTR.

In actual motion control, it is necessary to obtain all of the possible motion trajectories of the robot. All of the kinematic parameters of the points on the trajectory need to be obtained. Because of the redundant nature of the CCR, the CCR can reach the same point with different attitudes. All of the kinematic parameters corresponding to each pose are listed in an array. When solving, it is stipulated that the position information of the point is already known. The kinematic parameters of all the poses that can reach this point need to be solved.

Let the position information of the point at the end of the robot be $P_e [x_e \ y_e \ z_e]^T$. R_e is the pose information of the point. The equation that is to be solved for the inverse kinematics can be expressed as Equation (10).

$$P_e = \begin{bmatrix} ((c\theta_2 - 1)(s\varphi_1 s\varphi_2 + c\theta_1 c\varphi_1 c\varphi_2) + s\theta_2 s\theta_1 c\varphi_1)/k - L_1 c\varphi_1 (c\theta_1 - 1)/\theta_1 \\ ((c\theta_2 - 1)(c\varphi_1 s\varphi_2 + c\theta_1 s\varphi_1 c\varphi_2) - s\theta_2 s\theta_1 s\varphi_1)/k - L_1 s\varphi_1 (c\theta_1 - 1)/\theta_1 \\ ((c\theta_2 - 1)s\theta_1 c\varphi_2 + s\theta_2 c\theta_1)/k + L_1 s\theta_1/\theta_1 \end{bmatrix} \quad (10)$$

Assuming the pose is known, transform the pose into equations related to the kinematic parameters.

$$R_e(\varphi_1, \theta_1, \varphi_2, L_2) = R_s \quad (11)$$

To eliminate the redundant nature of Equation (10), Equation (11) is introduced to solve the inverse kinematics of the CCR. Let the known terminal pose be R_s and let R_e be the pose expression solved in Equation (7). By traversing all possible R_s values, the inverse kinematics of the setpoint can be solved by the LM algorithm. The iterative equation is shown in Equations (12) and (13):

$$q_{n+1} = q_n + H_n^{-1} g_n \quad (12)$$

$$H_k = J_k^T W_E J_k + W_N \quad (13)$$

The LM algorithm can obtain an inverse kinematics solution of the continuum robot. The geometric properties of the continuum robot show that its inverse kinematics solution is symmetric, as shown in Figure 7. Therefore, another solution can be obtained by exploiting the symmetry of the continuum robot.

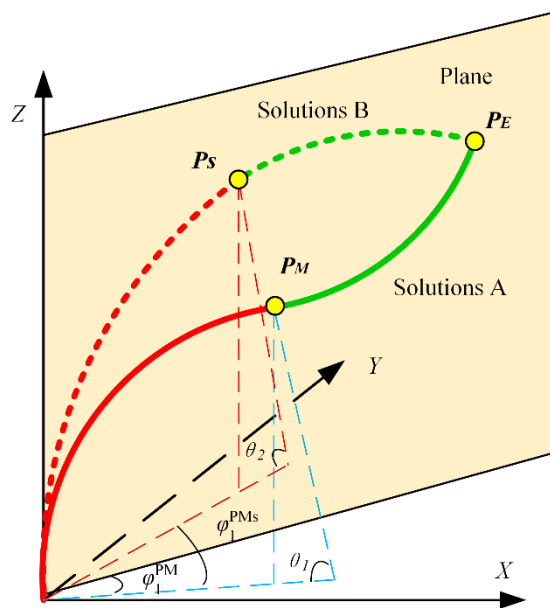


Figure 7. Two symmetric solutions at P_EOZ .

Assuming that one of the solutions A $(\varphi_1^{PM}, \theta_1, \varphi_2^{PM}, L_2^{PM})$ is known, the midpoint of the continuum robot shape corresponding to this solution is P_M . The midpoint refers to the endpoint of the NCR portion. Let the parameter of its symmetrical solution be B $(\varphi_1^{Ps}, \theta_2, \varphi_2^{Ps}, L_2^{Ps})$ and the midpoint of the corresponding continuum robot be P_S . A can be solved by the symmetry of the continuum robot:

$$\varphi_1^{Ps} = 2\varphi_{PE} - \varphi_1^{PM} \tag{14}$$

From Equation (15), other parameters can be obtained:

$$F(\varphi_2^{Ps}, L_2^{Ps}) = \begin{cases} x_e = ((c(kL_2^{Ps}) - 1)(s\varphi_1s\varphi_2^{Ps} + c\theta_1c\varphi_1c\varphi_2^{Ps}) + s(kL_2^{Ps})s\theta_1c\varphi_1)/k - L_1c\varphi_1(c\theta_1 - 1)/\theta_1 \\ z_e = ((c(kL_2^{Ps}) - 1)s\theta_1c\varphi_2^{Ps} + s(kL_2^{Ps})c\theta_1)/k + L_1s\theta_1/\theta_1 \end{cases} \tag{15}$$

3.3. Dexterity Evaluation and Optimization

Dexterity is one of the general evaluation indexes of robots. The commonly used dexterity evaluation methods of continuum robots include the condition number, end attitude angle, etc. The dexterity of the continuum robot was evaluated based on the condition number by Wang et al. [36]. The existing research shows that the evaluation method based on the condition number examines the uniformity of the robot Jacobian transformation matrix in all directions [37]. This method cannot intuitively describe the performance of the robot. In 2016, the continuum robot’s dexterity was evaluated based on a posture dexterity evaluation method that uses forward kinematics to compute the dexterity index by Wu [38]. This method can intuitively express the dexterity of the continuum robot. In this paper, the forward kinematics-based pose dexterity evaluation method is adopted.

In the pose dexterity assessment method, the dexterity of a point is defined as the number of poses the robot can achieve at that point, as shown in Figure 8. For statistical convenience, the number of all poses of that point (usually a ball) is taken as the denominator. The greater the number of poses a robot can achieve at a certain point, the more actions the robot can perform.

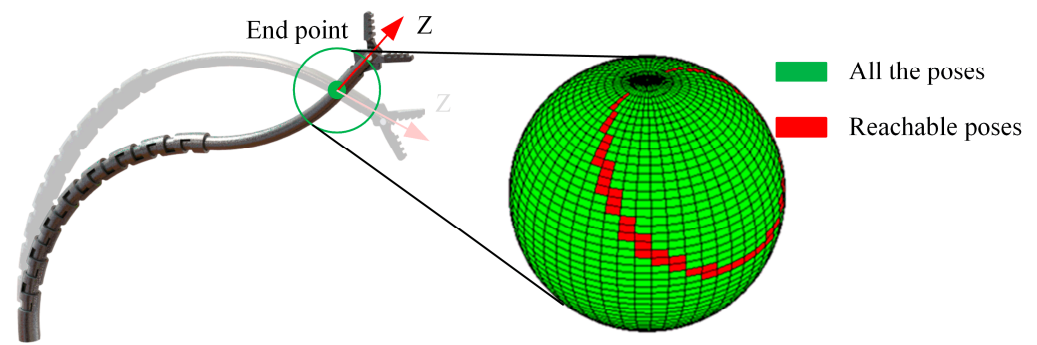


Figure 8. Cross-section of the robot workspace under the current configuration.

The end pose of the robot is represented by θ_0 and φ_0 in the Cartesian coordinate system. The end posture of the CCR can be expressed by Equation (16).

$$R_z = Rotx(\theta_0)Rotz(\varphi_0) \quad (16)$$

The $Rotz(\varphi_0)$ is the rotation matrix around the X-axis. The $Rotx(\theta_0)$ is the rotation matrix around the Z-axis. The X-axis and Z-axis are divided into n_1 and n_2 parts. The dexterity of the point can be represented by the graph which the X-axis and Z-axis form. Using the graph, the dexterity value of this point can be calculated using Equation (17).

$$a_{\text{point}} = \frac{n_p}{n_1 n_2} \quad (17)$$

In Equation (17), n_p is the number of shares of θ_0 and φ_0 in the dexterity graph obtained by solving the inverse solution at this point. Then, the dexterity value of the entire workspace can be expressed by Equation (18).

$$DI = \frac{\sum_1^N a_{\text{point}}}{N} \quad (18)$$

In Equation (18), DI is called the global dexterity index of the robot in this configuration. The numerical calculation of dexterity here does not consider the moving of the base coordinates. When the moving of the base coordinates is introduced, the dexterity value at this point can be calculated using Equation (19).

$$a_{\text{point}}^h = \frac{n_p^h}{n_1 n_2} \quad (19)$$

where h is the distance of the feed. n_p^h is the number of shares in the dexterity map with all of the CCR's end poses under a given feed distance.

After obtaining the dexterity values of the CCRs with different length configurations, the fruit fly algorithm Toolbox of MATLAB2018b was used to optimize the length configuration of the CCRs.

4. Results and Discussion

This section simulates the properties of the CCR using the method in Section 3. All the results are analyzed and discussed. The simulations in this section were all done in MATLAB 2018b. First, the smooth workspace of the CCR was drawn. The comparison with the other continuum robot workspaces was used to demonstrate the advantages of the CCR in the workspace. Then, the dexterity map of the CCR was drawn. A comparison of the dexterities of different continuum robots was proposed. Finally, using MATLAB's FOA toolbox, the length configuration of the CCR was optimized.

4.1. Workspace

According to Equations (7)–(9), the relationship between the maximum bending angle of the NCR and the length of each part can be shown in Figure 9 when the stability is considered. The maximum angle of the NCR is limited to π due to the mechanical structure limitation.

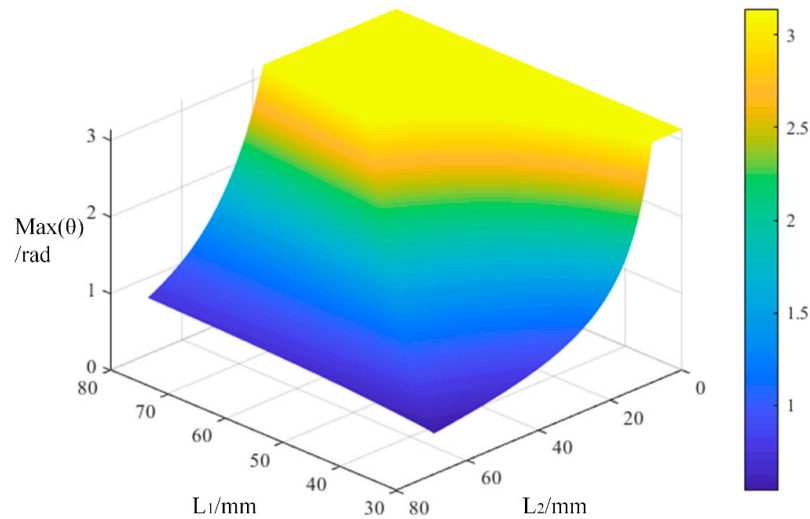


Figure 9. The relationship between the maximum bending angle of the NCR part and the length of each part.

Set the length of the CCR to be 50 mm long for the NCR part and 50 mm for the CTR part. As shown in Figure 10, the workspaces of those robots are drawn by the Monte Carlo method. Figure 10a is the workspace of the CCR considering the stability problem and the workspace without considering the stability problem (CCRF). It can be seen that the curvature of the edge portion of the CCRF exceeds the maximum curvature limit. Movement in this region can cause instability in the CTR portion. As shown in Figure 10b, the workspaces of the NCR are more three-dimensional, and the workspaces of the CTR are flatter. The reachable points of the NCR are concentrated at the far end of the robot. The reachable points of the CCR are concentrated in the middle part, and the reachable points of the CTR are focused on the end. This means that, under the same configuration, all three robots have good motion accuracy at the distal, middle and proximal end, respectively.

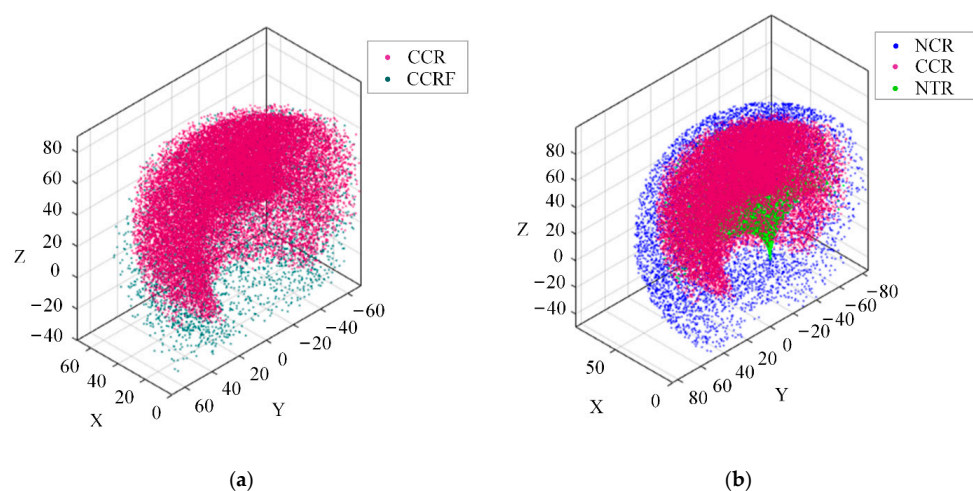


Figure 10. Workspace comparison of continuum robots. (a) The workspace considering the stability problem and the workspace without considering the stability problem, (b) The workspaces of different continuum robots.

4.2. Dexterity Comparison between the CTR and CCR

A total of 20 million groups of parameters were used to randomly operate the forward kinematics so that there were enough poses to reach the same point. With enough data, it can be directly considered that the poses obtained at this time are all attainable poses. Calculate the dexterity index of all the points in the workspace. The dexterity distribution graph is drawn using the dexterity values of these points, as shown in Figure 11.

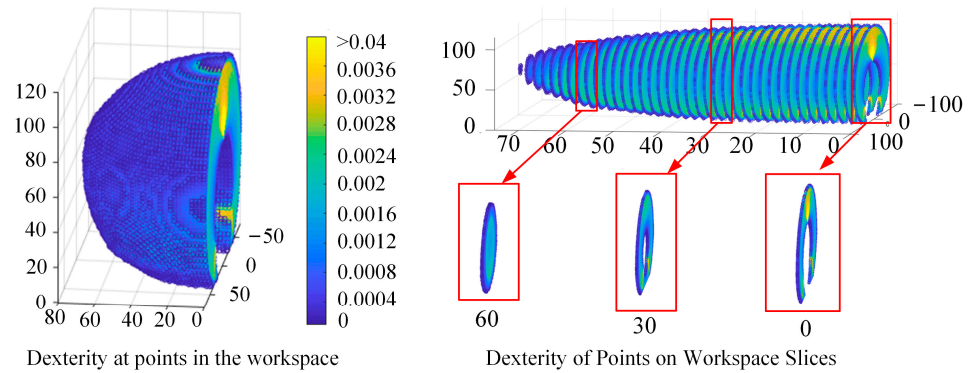


Figure 11. The dexterity distribution chart under the current configuration.

Figure 11 shows that the area with good dexterity is mainly concentrated in the middle of the robot’s workspace. The points with poor dexterity are focused on the edge of the workspace. By avoiding the movement of the robot to the edge, the robot has excellent dexterity.

The global dexterity index of the CTR with the same configuration is calculated. The global dexterity index of the CCR and CTR is shown in Table 4.

Table 4. The dexterity index of the CCR and TCM.

	Total Length	Length of the NCR Part	Length of the TCR Part	k of the TCR Part	Global Dexterity
CCR	100	50	50	$\pi/100$	0.0159
CTR	100	-	50–50	$\pi/100$	0.0108

As can be seen in Table 4, the global dexterity index of the CTR is 0.0108. The dexterity index of the CCR is 1.472 times that of the CTR. The results show that the dexterity of the CTR can be improved significantly by the CCR. The dexterity graph of the CCR is shown in Figure 12. It shows that the dexterity of the CCR is improved compared with the CTR. More importantly, the high dexterity points of the CCR are more evenly distributed, and the points inside the workspace have better dexterity. The points of poor dexterity are distributed on the workspace surface.

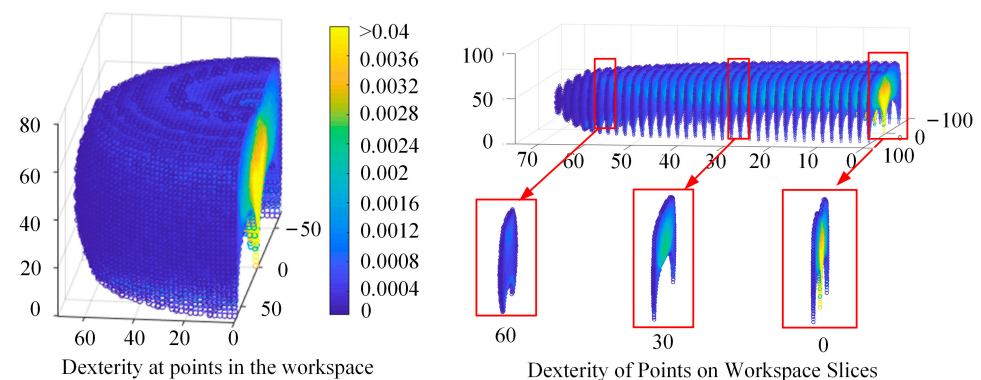


Figure 12. The dexterity performance of the CTR.

4.3. Length Distribution Optimization

The parameters and dexterity indexes for the CCR with different lengths can be found in Table 5. A total of 50 million points were introduced to calculate the dexterity indexes of the CCR under different length configurations.

Table 5. The dexterity indices of the CCR with different length ratios.

	Segment 1			Segment 2			Dexterity Index (DI)
	θ_1/rad	φ_1/rad	L_1/mm	L_2 (mm)	φ_2/rad	$k/(\text{rad}/\text{mm})$	
Group 1	$[0, \theta_{g1}]$	$[0, 2\pi]$	35	$[0, 65]$	$[0, 2\pi]$	$\pi/100$	0.0156
Group 2	$[0, \theta_{g2}]$	$[0, 2\pi]$	40	$[0, 60]$	$[0, 2\pi]$	$\pi/100$	0.0168
Group 3	$[0, \theta_{g3}]$	$[0, 2\pi]$	45	$[0, 55]$	$[0, 2\pi]$	$\pi/100$	0.0170
Group 4	$[0, \theta_{g4}]$	$[0, 2\pi]$	50	$[0, 50]$	$[0, 2\pi]$	$\pi/100$	0.0159
Group 5	$[0, \theta_{g5}]$	$[0, 2\pi]$	55	$[0, 45]$	$[0, 2\pi]$	$\pi/100$	0.0135
Group 6	$[0, \theta_{g6}]$	$[0, 2\pi]$	60	$[0, 40]$	$[0, 2\pi]$	$\pi/100$	0.0123
Group 7	$[0, \theta_{g7}]$	$[0, 2\pi]$	65	$[0, 35]$	$[0, 2\pi]$	$\pi/100$	0.0123
Group 8	$[0, \theta_{g8}]$	$[0, 2\pi]$	70	$[0, 30]$	$[0, 2\pi]$	$\pi/100$	0.0123
Group 9	$[0, \theta_{g9}]$	$[0, 2\pi]$	75	$[0, 25]$	$[0, 2\pi]$	$\pi/100$	0.0122

The total length of the robot is set as $L_m = 100$ mm. The curvature of the CTR is set as $\pi/100$, and the maximum bending angle of the NCR is set as π . The global dexterity of the robots with different length distributions is calculated using the method proposed in Section 3.3. The dexterity graphs of CCRs configured with different lengths can be found in Figure 13.

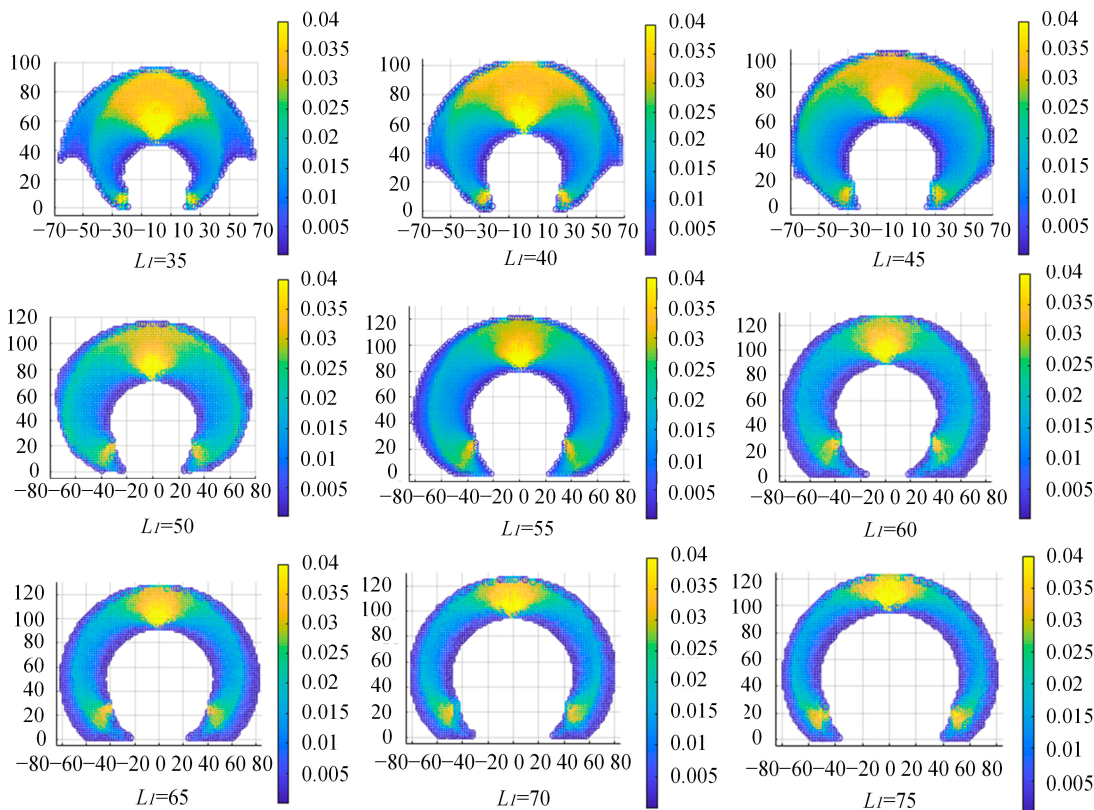


Figure 13. The dexterity of the continuum robot with different length distributions.

In Table 5, $\theta_{gi} = u_{1i}L_{1i}\theta_{gi}$ is the maximum allowable bending angle of the NCR part (segment 1) in the stable operation of the CCR. Due to physical constraints, θ_{gi} is a maximum of π . u_{1i} can be calculated from Equations (7)–(9). i is the i th group of simulations.

The smoothing spline of the MATLAB Fitting Toolbox is used to fit the relationship between L and the dexterity index, as shown in Figure 14. A fruit fly optimization algorithm (FOA) was used to optimize the CCR length assignment for optimal dexterity. The result of the optimization is shown in Figure 15. After optimization, the CCR has the optimal dexterity when the length of the NCR part is 44.3032 mm. To facilitate processing, we select integers, and the length of the NCR part is 44 mm. The global dexterity index is 0.0170.

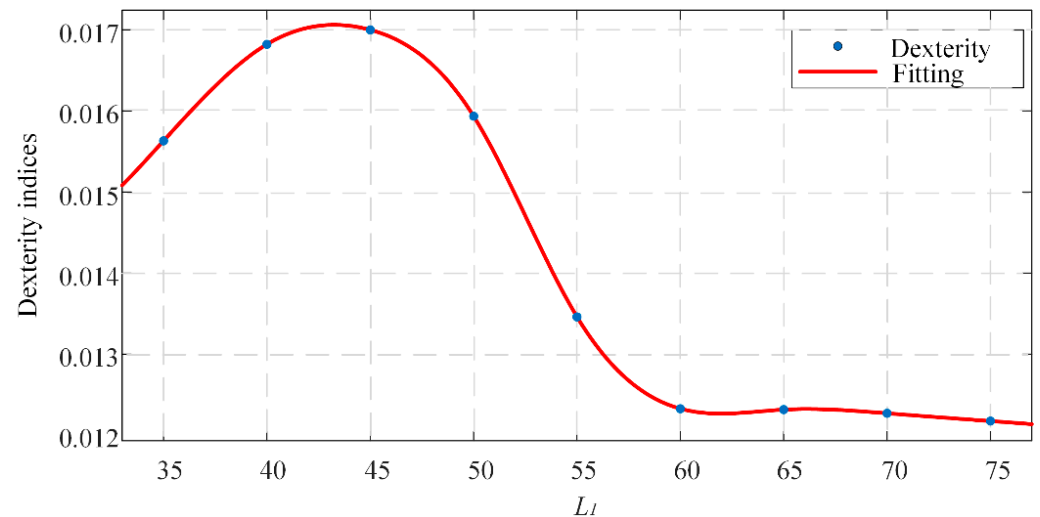


Figure 14. Fitted model.

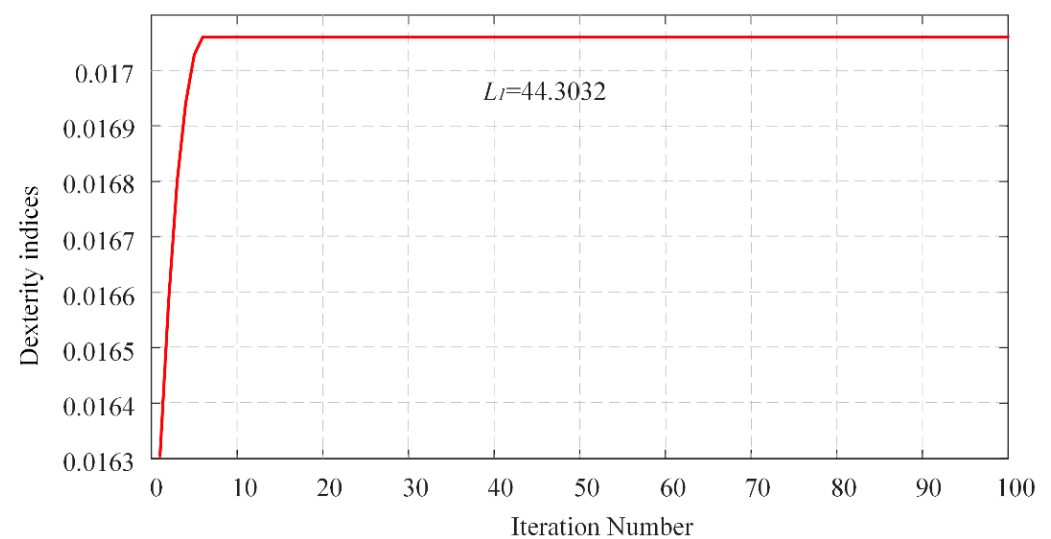


Figure 15. FOA-based dexterity index optimization.

The dexterity distribution diagram of the CCR is shown in Figure 16. Comparing Figures 12 and 16, the improved dexterity index is 7.4% after optimization. The CCR has good dexterity under the originally set length configuration. Compared with the CCR under other configurations, the dexterity index is significantly improved. For example, when the robot is configured with 65 mm (NCR part) and 35 mm (CTR part), $DI = 0.0123$. Its dexterity is increased by 38.2%.

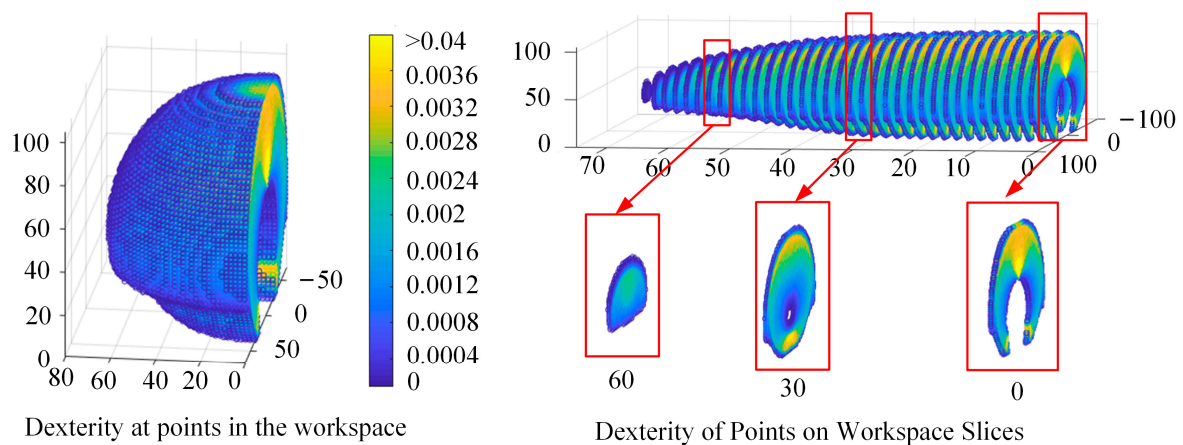


Figure 16. The dexterity after optimization.

5. Conclusions

To meet the requirements of minimally invasive surgery, a bio-inspired composite continuum robot (CCR) that combines the features of the NCR and CTR is proposed in this paper. Unlike other continuum robots, the CCR enables smaller diameters and larger central cavities. Then, to avoid unstable phenomena such as the ‘bifurcation’ of the CCR during operation, a stability limit is introduced to limit the maximum value of the bending angle of the NCR part. A kinematic model considering the stable motion conditions of the continuum robot is established. The workspace of the CCR is compared to the workspace of the NCR and CTR. The workspace of the CCR is significantly larger than that of the CTR. Then, the dexterity of the CCR is evaluated with an attitude angle-based evaluation method. The simulation shows that the dexterity index of the CCR was 2.32 times higher than that of the CTR. Finally, based on the dexterity index, the length distribution of the CCR was optimized using a fruit fly algorithm. The optimization results show that when the length of the CCR is configured as 44 mm (NCR part) and 56 mm (CTR part), it has the best dexterity. The dexterity value of the optimized CCR is 0.0170. The proposal of the CCR makes it possible to develop small-sized surgical instruments with a large central channel. It is ideal for minimally invasive procedures such as those for the skull base, lungs and heart.

In subsequent research, the authors will study the dynamics and statics of the CCR, study the tremor caused by CTR motion and build a corresponding experimental platform to verify the performance of the proposed model.

Author Contributions: Conceptualization, G.Z. and F.D.; methodology, G.Z.; software, S.X.; formal analysis, H.C. and X.Z.; resources, Y.L., R.S. and F.D.; data curation, G.Z.; writing—original draft preparation, G.Z.; writing—review and editing, F.D.; visualization, G.Z. and S.X.; supervision, Y.L., R.S. and F.D.; project administration, F.D.; funding acquisition, F.D. All authors have read and agreed to the published version of the manuscript.

Funding: This work was supported by the China Postdoctoral Science Foundation funded project (Grant No. 2019M662346), the Shandong Provincial Postdoctoral Innovative Talents Funded Scheme (Grant No. 238226), the Focus on Research and Development Plan in Shandong Province (Grant No. 2022CXGC010503), the Intelligent Robots and Systems High-Precision Innovation Center Open Fund (Grant No. 2019IRS06), the Fundamental Research Funds for the Central Universities and the Young Scholars Program of Shandong University.

Data Availability Statement: Not applicable.

Conflicts of Interest: The authors declare no conflict of interest.

References

1. Da Veiga, T.; Chandler, J.; Lloyd, P.; Pittiglio, G.; Wilkinson, N.J.; Hoshiar, A.K.; Harris, R.A.; Valdastrì, P. Challenges of continuum robots in clinical context: A review. *Prog. Biomed. Eng.* **2020**, *2*, 032003. [\[CrossRef\]](#)
2. Kolachalama, S.; Lakshmanan, S. Continuum Robots for Manipulation Applications: A Survey. *J. Robot.* **2020**, *2020*, 4187048. [\[CrossRef\]](#)
3. Li, S.; Hao, G. Current Trends and Prospects in Compliant Continuum Robots: A Survey. *Actuators* **2021**, *10*, 145. [\[CrossRef\]](#)
4. Lu, J.; Du, F.; Yang, F.; Zhang, T.; Lei, Y.; Wang, J. Kinematic modeling of a class of n-tendon continuum robots. *Adv. Robot.* **2020**, *34*, 1254–1271. [\[CrossRef\]](#)
5. Püschel, A.; Schafmayer, C.; Groß, J. Robot-assisted techniques in vascular and endovascular surgery. *Langenbeck's Arch. Surg.* **2022**, *1–7*. [\[CrossRef\]](#) [\[PubMed\]](#)
6. Iwasa, T.; Nakadate, R.; Onogi, S.; Okamoto, Y.; Arata, J.; Oguri, S.; Ogino, H.; Ihara, E.; Ohuchida, K.; Akahoshi, T.; et al. A new robotic-assisted flexible endoscope with single-hand control: Endoscopic submucosal dissection in the ex vivo porcine stomach. *Surg. Endosc.* **2018**, *32*, 3386–3392. [\[CrossRef\]](#)
7. Lei, Y.; Li, Y.; Song, R.; Du, F. Development of a novel deployable arm for natural orifice transluminal endoscopic surgery. *Int. J. Med Robot. Comput. Assist. Surg.* **2021**, *17*, e2232. [\[CrossRef\]](#)
8. Almendárez, M.; Alvarez-Velasco, R.; Pascual, I.; Alperi, A.; Moris, C.; Avanzas, P. Transseptal puncture: Review of anatomy, techniques, complications and challenges, a critical view. *Int. J. Cardiol.* **2022**, *351*, 32–38. [\[CrossRef\]](#)
9. Seung, S.; Liu, P.; Park, S.; Park, J.-O.; Ko, S.Y. Single-port robotic manipulator system for brain tumor removal surgery: SiromanS. *Mechatronics* **2015**, *26*, 16–28. [\[CrossRef\]](#)
10. Seetohul, J.; Shafiee, M. Snake Robots for Surgical Applications: A Review. *Robotics* **2022**, *11*, 57. [\[CrossRef\]](#)
11. Burgner-Kahrs, J.; Rucker, D.C.; Choset, H. Continuum Robots for Medical Applications: A Survey. *IEEE Trans. Robot.* **2015**, *31*, 1261–1280. [\[CrossRef\]](#)
12. Li, Z.; Du, R.; Lei, M.C.; Yuan, S.M. Design and analysis of a biomimetic wire-driven robot arm. In Proceedings of the ASME International Mechanical Engineering Congress and Exposition, Denver, CO, USA; 2011; Volume 54938, pp. 91–198.
13. Li, Z.; Du, R. Design and Analysis of a Bio-Inspired Wire-Driven Multi-Section Flexible Robot. *Int. J. Adv. Robot. Syst.* **2013**, *10*, 209. [\[CrossRef\]](#)
14. Li, Z.; Du, R.; Yu, H.; Ren, H. Statics modeling of an underactuated wire-driven flexible robotic arm. In Proceedings of the 5th IEEE RAS/EMBS International Conference on Biomedical Robotics and Biomechatronics, Sao Paulo, Brazil, 12–15 August 2014; pp. 326–331.
15. Xu, K.; Simaan, N. An Investigation of the Intrinsic Force Sensing Capabilities of Continuum Robots. *IEEE Trans. Robot.* **2008**, *24*, 576–587. [\[CrossRef\]](#)
16. Simaan, N.; Xu, K.; Wei, W.; Kapoor, A.; Kazanzides, P.; Taylor, R.; Flint, P. Design and Integration of a Telerobotic System for Minimally Invasive Surgery of the Throat. *Int. J. Robot. Res.* **2009**, *28*, 1134–1153. [\[CrossRef\]](#)
17. Wilkening, P.; Alambeigi, F.; Murphy, R.J.; Taylor, R.H.; Armand, M. Development and Experimental Evaluation of Concurrent Control of a Robotic Arm and Continuum Manipulator for Osteolytic Lesion Treatment. *IEEE Robot. Autom. Lett.* **2017**, *2*, 1625–1631. [\[CrossRef\]](#)
18. Gao, A.; Murphy, R.J.; Liu, H.; Iordachita, I.I.; Armand, M. Mechanical Model of Dexterous Continuum Robots with Compliant Joints and Tendon/External Force Interactions. *IEEE/ASME Trans. Mechatron.* **2017**, *22*, 465–475.
19. Murphy, R.J.; Kutzer, M.D.; Segreti, S.M.; Lucas, B.C.; Armand, M. Design and kinematic characterization of a surgical robot with a focus on treating osteolysis. *Robotica* **2014**, *32*, 835–850. [\[CrossRef\]](#)
20. Wang, H.; Wang, X.; Yang, W.; Du, Z. Design and kinematic modeling of a notch continuum robot for laryngeal surgery. *Int. J. Control. Autom. Syst.* **2020**, *18*, 2966–2973. [\[CrossRef\]](#)
21. Francis, P.; Eastwood, K.W.; Bodani, V.; Looi, T.; Drake, J.M. Design, Modelling and Teleoperation of a 2 mm Diameter Compliant Instrument for the da Vinci Platform. *Ann. Biomed. Eng.* **2018**, *46*, 1437–1449. [\[CrossRef\]](#)
22. Webster, I.R.J.; Romano, J.M.; Cowan, N.J. Mechanics of Precurved-Tube Continuum Robots. *IEEE Trans. Robot.* **2008**, *25*, 67–78. [\[CrossRef\]](#)
23. Bruns, T.L.; Ramirez, A.A.; Emerson, M.A.; Lathrop, R.A.; Mahoney, A.W.; Gilbert, H.B.; Liu, C.L.; Russell, P.T.; Labadie, R.F.; Weaver, K.D.; et al. A modular, multi-arm concentric tube robot system with application to transnasal surgery for orbital tumors. *Int. J. Robot. Res.* **2021**, *40*, 521–533. [\[CrossRef\]](#)
24. Bergeles, C.; Gosline, A.H.; Vasilyev, N.V.; Codd, P.J.; Del Nido, P.J.; Dupont, P.E. Concentric Tube Robot Design and Optimization Based on Task and Anatomical Constraints. *IEEE Trans. Robot.* **2015**, *31*, 67–84. [\[CrossRef\]](#) [\[PubMed\]](#)
25. Swaney, P.J.; Mahoney, A.W.; Hartley, B.I.; Ramirez, A.A.; Lamers, E.; Feins, R.H.; Alterovitz, R.; Webster, I.R.J. Toward Transoral Peripheral Lung Access: Combining Continuum Robots and Steerable Needles. *J. Med. Robot. Res.* **2017**, *2*, 17500015. [\[CrossRef\]](#)
26. AlFalahi, H.; Renda, F.; Stefanini, C. Concentric Tube Robots for Minimally Invasive Surgery: Current Applications and Future Opportunities. *IEEE Trans. Med Robot. Bionics* **2020**, *2*, 410–424. [\[CrossRef\]](#)
27. Greer, J.D.; Morimoto, T.K.; Okamura, A.M.; Hawkes, E.W. Series pneumatic artificial muscles (sPAMs) and application to a soft continuum robot. In Proceedings of the IEEE International Conference on Robotics and Automation, Singapore, 29 May–3 June 2017. [\[CrossRef\]](#)

28. Laschi, C.; Cianchetti, M.; Mazzolai, B.; Margheri, L.; Follador, M.; Dario, P. Soft Robot Arm Inspired by the Octopus. *Adv. Robot.* **2012**, *26*, 709–727. [[CrossRef](#)]
29. Dupont, P.; Simaan, N.; Choset, H.; Rucker, C. Continuum Robots for Medical Interventions. *Proc. IEEE* **2022**, 1–24. [[CrossRef](#)]
30. Li, Z.; Wu, L.; Ren, H.; Yu, H. Kinematic comparison of surgical tendon-driven robots and concentric tube robots. *Mech. Mach. Theory* **2017**, *107*, 148–165. [[CrossRef](#)]
31. Abdel-Nasser, M.; Salah, O. New continuum surgical robot based on hybrid concentric tube-tendon driven mechanism. *Proc. Inst. Mech. Eng. Part C J. Mech. Eng. Sci.* **2021**, *235*, 7550–7568. [[CrossRef](#)]
32. Rucker, C.; Childs, J.; Molaie, P.; Gilbert, H.B. Transverse Anisotropy Stabilizes Concentric Tube Robots. *IEEE Robot. Autom. Lett.* **2022**, *7*, 2407–2414. [[CrossRef](#)]
33. Hannan, M.W.; Walker, I.D. Novel kinematics for continuum robots. In *Advances in Robot Kinematics*; Springer: Dordrecht, The Netherlands, 2000; pp. 227–238.
34. Xu, R.; Atashzar, S.F.; Patel, R.V. Kinematic instability in concentric-tube robots: Modeling and analysis. In Proceedings of the 5th IEEE RAS/EMBS International Conference on Biomedical Robotics and Biomechatronics, Sao Paulo, Brazil, 12–15 August 2014; pp. 163–168.
35. Dupont, P.E.; Lock, J.; Itkowitz, B.; Butler, E.J. Design and Control of Concentric-Tube Robots. *IEEE Trans. Robot.* **2010**, *26*, 209–225. [[CrossRef](#)]
36. Wang, J.; Lau, H.Y.K. Dexterity Analysis based on Jacobian and Performance Optimization for Multi-segment Continuum Robots. *J. Mech. Robot.* **2021**, *13*, 061012. [[CrossRef](#)]
37. Biyun, X.; Jing, Z. Advances in Robotic Kinematic Dexterity and Indices. *Mech. Sci. Technol.* **2011**, *30*, 1386–1393.
38. Wu, L.; Crawford, R.; Roberts, J. Dexterity Analysis of Three 6-DOF Continuum Robots Combining Concentric Tube Mechanisms and Cable-Driven Mechanisms. *IEEE Robot. Autom. Lett.* **2016**, *2*, 514–521. [[CrossRef](#)]